HHS Public Access

Author manuscript

Inorg Chem. Author manuscript; available in PMC 2022 February 15.

Published in final edited form as:

Inorg Chem. 2021 February 15; 60(4): 2168–2177. doi:10.1021/acs.inorgchem.0c02688.

Manganese(II)-Based Responsive Contrast Agent Detects Glucose-Stimulated Zinc Secretion from the Mouse Pancreas and Prostate by MRI

Sara Chirayil[#],
Advanced Imaging Research Center, University of Texas Southwestern Medical Center, Dallas, Texas 75390, United States

Veronica Clavijo Jordan[#],
Advanced Imaging Research Center, University of Texas Southwestern Medical Center, Dallas, Texas 75390, United States; Athinoula A. Martinos Center for Biomedical Imaging, Massachusetts General Hospital, Harvard Medical School, Charlestown, Massachusetts 02129, United States

André F. Martins[#],
Advanced Imaging Research Center, University of Texas Southwestern Medical Center, Dallas, Texas 75390, United States; Werner Siemens Imaging Center, Eberhard Karls University Tübingen, Tübingen 72076, Germany; Cluster of Excellence iFIT (EXC 2180), "Image-Guided and Functionally Instructed Tumor Therapies", University of Tübingen, Tübingen 72076, Germany; Department of Chemistry, University of Texas at Dallas, Richardson, Texas 75080, United States

Namini Paranawithana,
Department of Chemistry, University of Texas at Dallas, Richardson, Texas 75080, United States

S. James Ratnakar,
Advanced Imaging Research Center, University of Texas Southwestern Medical Center, Dallas, Texas 75390, United States

A. Dean Sherry
Advanced Imaging Research Center, University of Texas Southwestern Medical Center, Dallas, Texas 75390, United States; Department of Chemistry, University of Texas at Dallas, Richardson, Texas 75080, United States

[#] These authors contributed equally to this work.

Corresponding Author: A. Dean Sherry – *Advanced Imaging Research Center, University of Texas Southwestern Medical Center, Dallas, Texas 75390, United States; Department of Chemistry, University of Texas at Dallas, Richardson, Texas 75080, United States*; dean.sherry@utsouthwestern.edu, sherry@utdallas.edu.

ASSOCIATED CONTENT

Supporting Information

The Supporting Information is available free of charge at https://pubs.acs.org/doi/10.1021/acs.inorgchem.0c02688.

Experimental section of this manuscript, materials and methods, additional supporting results, synthesis of Mn complex, competition binding curve, transverse ^{17}O relaxivity, best-fit parameters obtained by analysis of the ^{17}O NMR data, *In vivo* MRI at 4.7 T and 9.4 T, and LC-MS of background urine and bile (PDF)

The authors declare no competing financial interest.

Complete contact information is available at: https://pubs.acs.org/10.1021/acs.inorgchem.0c02688

Abstract

A Mn(II)-based zinc-sensitive MRI contrast agent, MnPyC3A–BPEN, was prepared, characterized, and applied in imaging experiments to detect glucose-stimulated zinc secretion (GSZS) from the mouse pancreas and prostate *in vivo*. Thermodynamic and kinetic stability tests showed that MnPy-C3A–BPEN has superior kinetic inertness compared to GdDTPA, is less susceptible to transmetalation in the presence of excess Zn^{2+} ions, and less susceptible to transchelation by albumin. In comparison with other gadolinium-based zinc sensors bearing a single zinc binding moiety, MnPyC3A–BPEN appears to be a reliable alternative for imaging β-cell function in the pancreas and glucose-stimulated zinc secretion from the prostate.

Graphical Abstract

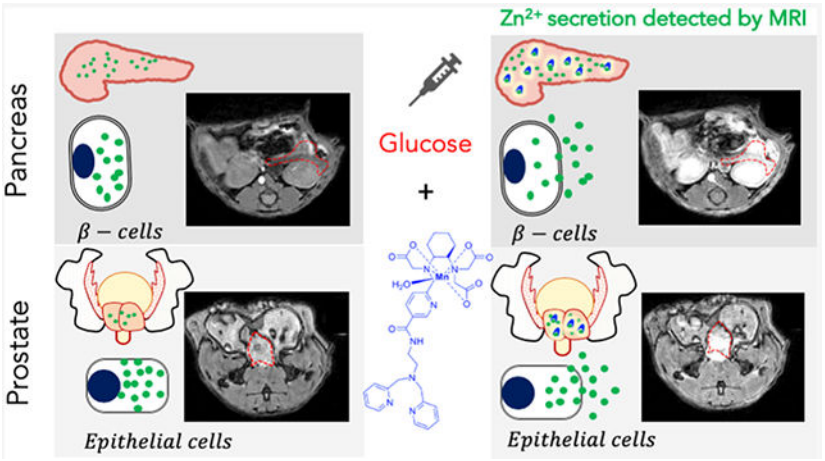

INTRODUCTION

Magnetic resonance imaging (MRI) has become arguably the most powerful imaging modality because of its outstanding spatial and temporal resolution, its versatility, and its ability to detect functional and molecular events in tissue.[1,2] Although MRI is less sensitive than PET, SPECT, and optical methods,[3,4] interest in developing new molecular probes that report on specific biological events continues to grow.[5] The implementation of more advanced techniques such as CEST and MR fingerprinting highlights the versatility of magnetic resonance.[6–9] Despite these major physics advances, interest in newer types of exogenous molecular contrast agents (CAs) remains strong. To date, the most widely used MRI CAs have been the gadolinium-based T_1 agents.[10] Although gadolinium-based CAs (GBCA) have been widely used since the introduction of Magnevist in 1988, the appearance of Nephrogenic Systemic Fibrosis (NSF) in 2006[11–13] and, more recently, reports of Gd^{3+} deposition in the brain[14,15] have raised concerns about continuing the use of GBCA.

These issues have been largely attributed to the poor kinetic inertness of Gd-complexes formed with acyclic ligands such as those in Gadodiamide and Gadoversetamide.[10,16,17] Nonetheless, the U.S. Food and Drug Administration (FDA) and the European Medicines Agency (EMA) raised concerns for all forms of GBCA including those derived from macrocyclic ligands. From this history, the scientific community has learned two principles;

first, there is a need to develop safe alternatives to acyclic GBCA and, second, the kinetic inertness and thermodynamic stability should be thoroughly investigated for every new metal-based agent developed for medical imaging purposes.

Manganese-based MRI agents are beginning to emerge as alternatives to gadolinium-based agents because of their favorable spin state, (S = 5/2 for most Mn^{2+} complexes), long longitudinal electronic relaxation times, and fast water exchange rates.[18] Moreover, manganese is generally considered to be less toxic because it is an endogenous metal ion and is quickly cleared *via* hepatobiliary excretion.[19,20] However, like any metal ion complexes injected in relatively high doses, Mn-complexes also have limitations. For example, if Mn^{2+} dissociates from a chelating ligand, free Mn^{2+} can catalyze the formation of reactive oxygen species (ROS) and reactive nitrogen species (RNS),[21–23] and some Mn^{2+} complexes have been shown to mimic mitochondrial manganese superoxide dismutase (MnSOD). The first and only Mn^{2+} complex approved for human injection, $Mn(DPDP)^{3-}$ (Teslascan), is no longer commercially available because of unfavorable side effects and subsequent lack of use.[24–26] Historically, Mn^{2+} was one of the first paramagnetic ions considered for use as T_1-based CA for MRI but insufficient ligand field stabilization provided by most ligands makes the development of suitable manganese complexes for medical imaging quite challenging.[27] However, a renewed interest in Mn^{2+} has led to the development of newer types of ligands for optimal chelation, some derived from macrocyclic ligands and others from acyclic ligands. Both types vary in (i) thermodynamic stability, (ii) kinetic inertness, (iii) number of inner-sphere water molecules (q), (iv) water exchange rates (k_{ex}), (v) binding interactions with plasma proteins, (vi) oxidation (Mn^{2+}/Mn^{3+}), and (vii) general versatility.[20,28–36] Among the most promising Mn^{2+} chelates reported so far are those bearing picolyl coordinating groups attached to either a macrocyclic or acyclic amine.[37,38] This is the case for Mn(*N*-picolyl-*N,N′,N′*-trans-1,2-cyclo-hexylenediaminetriacetate hydrate, [MnPyC3A·$(H_2O)^-$], a recently reported complex having a r_1 relaxivity comparable to commercially available GBCA that also displays rapid hepatobiliary/renal clearance *in vivo* and low toxicity.[20] A peptide-conjugated version of this agent has also been used to target fibrin filaments in cardiac thrombus.[20,39]

Acyclic chelates such as in MnPyC3A·$(H_2O)^-$ undergo transmetalation when challenged with excess $ZnCl_2$ more easily than macrocyclic chelates but less easily when compared to linear GBCAs.[20] Transmetalation by Zn^{2+} is thought to be one of the main mechanisms for the release of Gd^{3+} from linear amine-based GBCA. Given the widespread interest in responsive MR CAs for the detection of local changes in freely available Zn^{2+} in the brain,[40,41] pancreas,[42–45] and prostate,[46,47] it is important to design zinc-sensitive agents in which Zn^{2+} does not displace the paramagnetic ion from the agent itself.[48–51] Our first zinc-sensitive agent, GdDOTA—diBPEN, was a macrocyclic 1,4,7,10-tetraazacyclododecane-1,4,7,10-tetraacetic acid (DOTA) derivative with two bispyridine (BPEN)-extended side chains for zinc recognition (Figure 1a).[45] When exposed to Zn^{2+}, the two BPEN moieties each bind a single Zn^{2+} ion and the resulting complex then forms a ternary complex with albumin. This protein interaction results in the reduced molecular rotation of the Gd^{3+} complex and a resulting increase in r_1 relaxivity and an increase in MR signal intensity in T_1-weighted images (Figure 1b). It was also shown that excess Zn^{2+} added to GdDOTA—diBPEN does not displace the Gd^{3+} ion from the macrocyclic ligand.

Given this prior information, we hypothesized that by conjugating a zinc recognition unit such as BPEN onto MnPyC3A, one might actually protect the Mn center against transmetalation by zinc while retaining the zinc-responsiveness of the agent.

We report here a comprehensive chemical–biophysical study of MnPyC3A–BPEN and demonstrate its potential as a zinc-sensitive MRI CA. Our overarching goal was to create an alternative to GdDOTA–diBPEN[42,52] or GdDO3A–BPEN[45] for the *in vivo* detection of glucose stimulated zinc secretion (GSZS) in the prostate and the pancreas by MRI. *In vivo* imaging comparisons of MnPyC3A–BPEN with GdDO3A–BPEN, a derivative bearing a single zinc binding side chain (Figure 1a), show that MnPyC3A–BPEN may indeed be a viable alternative for functional imaging of zinc secretion in both the mouse pancreas and prostate.

RESULTS

Synthesis.

Encouraged by the promising report of MnPyC3A·$(H_2O)^-$ as an imaging probe, we sought to use this same synthon as the basis of a new zinc-sensitive MRI agent. The synthetic route to this new derivative is outlined in Scheme 1. Compound **1** was prepared using reported protocols.[21] We took advantage of the pyridyl moiety to provide an easy and achiral means to incorporate the zinc binding moiety. The 5-position in the pyridyl moiety was functionalized for this purpose. *N′,N′-bis*(pyridine-2-ylmethyl)ethane-1,2-diamine (BPEN) was coupled to **1** followed by the de-protection of **2** which yielded **3** in reasonable yields. The zinc sensor MnPyC3A–BPEN was prepared by stirring **3** with $MnCl_2$ at pH 6.5.

Relaxometry and Binding Characteristics.

The T_1 relaxation efficiency of paramagnetic agents such as this are typically compared by their longitudinal relaxivity r_1 values as defined by eq 1.

$$r_1{}^p = \frac{1}{[M]}\left(\frac{1}{T_1{}^{\text{obs}}} - \frac{1}{T_1{}^{\text{dia}}}\right) \quad (1)$$

For zinc-responsive agents like MnPyC3A–BPEN, one must consider the r_1 values of several species including the agent itself, the binary MnPyC3A–BPEN·Zn^{2+} complex, and the ternary MnPyC3A–BPEN·Zn^{2+}•albumin complex. The r_1 values of MnPyC3A–BPEN ± Zn^{2+} and ±0.6 mM HSA are listed in Table 1 and compared with r_1 values previously reported for GdDO3A–BPEN. The data show that the r_1 of MnPyC3A–BPEN is slightly lower than GdDO3A–BPEN in the absence of Zn^{2+}, increases only slightly in the presence of one equivalent of Zn^{2+} but increases by 4-fold in the presence of both Zn^{2+} and HSA. These results parallel the r_1 changes previously reported for GdDO3A–BPEN. Although the relaxivity data reported in Table 1 are measured at 0.5 *T*, these values are magnetic field dependent, especially for those agents that bind to larger macromolecules. For comparison, the relaxivity values measured at 9.4 *T* are also reported in Table S1. Here, the differences between the binary (5.0 mM^{-1} s^{-1}) and ternary complexes (5.4 mM^{-1} s^{-1}) are less dramatic

but this small difference appears to be sufficient to detect release of Zn^{2+} *in vivo* (see below).

A titration of MnPyC3A–BPEN with Zn^{2+} showed that r_1 increases with incremental addition of Zn^{2+} ions until a 1:1 complex is formed then levels off with further addition of Zn^{2+}. The binding affinity of the BPEN unit on MnPyC3A–BPEN with Zn^{2+} was determined by competitive binding experiments with the Zn-sensitive fluorescence ligand, ZnAF–2F.[42,45] These titrations yielded a dissociation constant of $K_D = 93 \pm 4$ nM for Zn^{2+} binding with MnPyC3A–BPEN (Figure S1). These data show that the BPEN moiety retains a high affinity for Zn^{2+} when conjugated to MnPyC3A.

The number of inner-sphere water molecules (q) and the water exchange rate (k_{ex}) in MnPyC3A–BPEN were determined by simultaneous analysis of ^{17}O reduced T_2 data.[53–56] These data, summarized in Table 2 and Table S2, indicate that MnPyC3A–BPEN has a single inner-sphere water coordination site with an exchange rate ($k_{ex} = 0.7 \pm 0.1 \times 10^8\ s^{-1}$) similar to that reported for MnPyC3A.[20]

Albumin Binding Studies.

Albumin, the most abundant protein in plasma, plays an important role in the transport of drugs and the delivery of essential poorly soluble molecules to cells. Free Zn^{2+} ions also have a high affinity (29.5 nM) binding site on albumin,[57] an affinity about 3-fold stronger than the binding affinity between MnPyC3A–BPEN and Zn^{2+}.[42,58] This means that albumin must play a key role in the formation of the ternary complex involving Zn^{2+}.[45] At low-to-medium magnetic fields, r_1 is dominated by the rotational correlation time, τ_R, of the protein. This is clearly the case in our studies because r_1 relaxivity of MnPyC3A–BPEN is amplified upon the addition of both Zn^{2+} and 600 μM human serum albumin (HSA) (Table 1). In the presence of 600 μM HSA but no zinc, a modest increase in r_1 was observed. This demonstrates that MnPyC3A–BPEN alone, unlike GdDOTA–diBPEN or GdDO3A–BPEN, interacts weakly with HSA even in the absence of Zn^{2+} ions. An alternative explanation might be that some Mn^{2+} is released from the chelate (transchelation) and bound to a metal ion binding site on HSA. The r_1 data in general show that MnPyC3A–BPEN does respond to the presence of Zn^{2+} and HSA by showing an increase in r_1 similar to that reported for GdDO3A–BPEN.[52]

The binding of MnPyC3A–BPEN·Zn^{2+} with HSA was evaluated using two different methods: (1) a proton relaxation enhancement (PRE) titration and fluorescence titrations using dansylglycine, a drug site 2 binding molecule (Figure 2a,b). The K_D values obtained from these experiments yielded comparable binding affinities (Table 1). In a complex mixture containing a Mn-based zinc sensor, HSA, and Zn^{2+} ions, several species are present in the solution. The combined data suggest that HSA heavily mediates the amount of MnL_x–Zn^{2+}–HSA present in this mixture. This is due to the fact that HSA is normally present at a higher concentration in the plasma compared to Zn^{2+} (<20 μM) and also has a higher affinity for Zn^{2+} in comparison to BPEN-based sensors such as these.[42,57,59]

Kinetic Inertness.

PyC3A forms a complex with Mn^{2+} with moderate thermodynamic stability (log K_{MnL} = 14.14, p_{Mn} = 98.17).[20] and one would predict that PyC3A would form even more stable complexes with Zn^{2+} and Cu^{2+} as predicted by Irving–Williams theory.[60] Hence, the kinetic inertness of MnPyC3A–BPEN is quite important if one intends to use this agent as a reporter of Zn^{2+} release from tissues. To test this, the complex was first challenged by the addition of 25-fold excess Zn^{2+} to MnPyC3A–BPEN at pH 6.0, 37 °C while monitoring changes in water proton r_1 (Figure 2c). The data show that MnPyC3A–BPEN is quite inert to transmetalation by Zn^{2+} in comparison to GdDTPA which dissociates very quickly. A fit of these data to a pseudo-first-order kinetic model showed that MnPyC3A–BPEN was about 2-fold more inert toward transmetalation by Zn^{2+} ($k = 3.2 \times 10^{-4}$ s^{-1}) compared to the parent compound, MnPyC3A ($k = 6.7 \times 10^{-4}$ s^{-1}). This suggests that the BPEN moiety provides some protection against transmetalation of Mn^{2+} by excess Zn^{2+} even though it binds only one equivalent of Zn^{2+} ions.

Similarly, relaxometric data on samples containing 0.1 mM MnPyC3A–BPEN or MnPyC3A plus 0.6 mM HSA show that the former complex was somewhat less susceptible to transchelation by albumin (Figure 2d). Using the relaxivity values in Table 1 and the reported relaxivity of Mn^{2+} bound to albumin (97 mM^{-1} s^{-1}),[61] the amount of Mn^{2+} transchelated from MnPyC3A to HSA was estimated at ~2% over 1 h and ~12% over 13 h. Similar experiments with MnPyC3A–BPEN showed that slightly less Mn^{2+} moves from the chelate to HSA over this same time period (~2% over 1 h and ~8% over 13 h). This effect was also observed by ^{17}O NMR experiments which showed an increase in $q = 2.5 \pm 0.2$ in the presence of 1 equiv of Zn^{2+} and excess HSA (Figure S2, Table S2). Data also suggest that the presence of zinc and HSA favorably impacts q and k_{ex}, and the different species present in the solution contribute to the overall observed r_1 enhancement. Thus, it appears that having a BPEN moiety attached to the chelate protects against both transmetalation by Zn^{2+} and transchelation by HSA. The exact mechanism of this protection is yet to be investigated.

In Vivo MRI.

Several mouse imaging experiments were performed to evaluate the potential use of MnPyC3A–BPEN for detecting Zn^{2+} secretion from tissues *in vivo* by MRI. As shown previously, the pancreas co-releases insulin and Zn^{2+} after the bolus injection of glucose and that the increase in Zn^{2+} in the extracellular space of β-cells can be detected by MRI using a Gd-based zinc sensor. To date, this is the only reported method for imaging β-cell function *in vivo*.[43,52] More recently, GSZS was also observed in the prostate of fasted mice by MRI.[46,62] Although the molecular mechanism of GSZS from healthy prostate cells remains to be fully elucidated, this response has been shown to be useful for distinguishing healthy versus malignant prostate cells.[46,62,63] Figure 3a shows typical *in vivo* T_1-weighted MRI images of mice before and after a bolus injection of MnPyC3A–BPEN plus glucose. Contrast enhancement was quite evident in the pancreas and prostate after a bolus of glucose and no significant increase in signal intensity was seen in these organs in control mice receiving saline instead of glucose (Figure S3). Furthermore, the administration of MnPyC3A plus glucose instead of MnPyC3A–BPEN plus glucose showed little to no contrast enhancement

in either tissue (Figure S4). Together these experiments highlight the specific interactions between secreted Zn^{2+}, plasma albumin, and MnPyC3A–BPEN leading to the formation of the ternary complex. Conversely, MnPyC3A interacts only weakly with plasma proteins.[20] The % signal intensity gain after the injection of each agent in ROIs in the pancreas, prostate, kidneys, and liver normalized to muscle are shown in Figure 3b. These data show that significantly higher signal enhancement is observed after the injection of MnPyC3A–BPEN *versus* MnPyC3A not only in those tissues known to release Zn^{2+} (pancreas and prostate) but also in the liver and kidneys. For comparison purposes, the area-under-the curve (AUC) over the first 16 min post CA injection ($AUC^{0–16\ min}$) for each tissue are compared in Figure 3b. These results indicate that after glucose stimulation, MnPyC3A–BPEN induces a larger MR signal enhancement over the secretory period (0–16 min) in comparison to parent compound MnPyC3A. Figure 3b (inset) shows that the liver-to-kidney ratio for the two agents do not differ, consistent with equivalent excretion mechanisms for MnPyC3A–BPEN and MnPyC3A. Nevertheless, the observation that MnPyC3A–BPEN induces greater signal enhancement in all tissues compared to MnPyC3A delivered at the same dose indicates that MnPyC3A–BPEN circulates in all tissues as the higher relaxivity ternary MnPyC3A–BPEN·Zn^{2+}·albumin species.

Tissue Bio-Distribution.

Additional tissue biodistribution studies were performed in mice after the injection of MnPyC3A–BPEN. In these studies, either 0.07 mmol/kg MnPyC3A–BPEN, 0.04 mmol/kg $MnCl_2$, or saline were injected followed by an immediate injection of glucose. The kidney, brain, liver, heart, spleen, muscle, pancreas, and prostate were resected at either 15 or 90 min postinjection to monitor short-*versus* long-term accumulation and excretion. After tissue digestion, total Mn was measured by ICP–MS (Figure 4). In the $MnCl_2$ group, significant Mn was found in the kidney, liver, heart, and pancreas at 15 min postinjection but little at 90 min (Figure 4b), consistent with a previous report.[20] In the MnPyC3A–BPEN group, about 2- to 3-fold less Mn was found in any of these same tissues at 15 min postinjection, with the most found in the kidney and liver. At 90 min, the amount of Mn in the kidney and liver was reduced by ~60%. No significant Mn was found in the heart tissue in the MnPyC3A–BPEN group, consistent with stable chelation of Mn throughout. Given that the tissue biodistribution data showed comparable amounts of Mn in the kidney and liver after the injection of MnPyC3A–BPEN, this indicates that the excretion pathway is about 50% biliary and 50% renal. To evaluate this further, a separate cohort of mice were imaged serially after receiving 0.07 mmol/kg MnPyC3A–BPEN plus glucose. Figure 5a (left) shows coronal images of a mouse prior to and at 90 min postinjection. These images show once again that the agent is largely cleared from all tissues, including the kidney and liver, at 90 min but the gallbladder remained hyperintense consistent with hepatobiliary excretion of MnPyC3A–BPEN. Dynamic quantitative excretion information was obtained by analyzing the change in signal intensity in the respective excretory organs (Figure 5b). The signal change in the kidneys showed a maximum at 27 min postinjection, and only 25% of that signal was lost due to excretion after 90 min. On the other hand, the change in the liver signal postinjection also showed a maximum at 27 min, but at 90 min–89% of the signal was reduced because of the excretion of the compound and accumulation in the gallbladder. The gallbladder signal gradually increased and reached a plateau starting at 60 min and ending with a signal change

of 242 ± 68% after 90 min. To evaluate the integrity of MnPyC3A–BPEN after excretion *via* the two pathways, we collected bile from the gallbladder or duodenum and urine from the bladder 90 min postinjection. The LC–MS elution profiles of samples of bile and urine collected 90 min postinjection are shown in Figure 5c. The gallbladder showed an intense MR signal in T_1-weighted scans, and the bile LC–MS trace shows a peak at an elution time of ~11 min where the mass coincides with that of intact MnPyC3A–BPEN. Similarly, the LC–MS profile of urine showed a peak at ~14 min consistent with intact MnPyC3A–BPEN. To validate that the peaks we were observing were indeed the intact compound, we measured the Mn concentration collected from urine and bile 90 min post i.v. injection of MnPyC3A–BPEN by inductively coupled plasma mass spectrometry. Naïve urine and bile (see Figure S5 for chromatogram) were then spiked with an authentic sample of the original compound. The LC–MS chromatograms of spiked urine and bile both are consistent with the intact compound seen in the samples collected from urine and bile illustrated in Figure 5c. These results suggest that MnPyC3A–BPEN is largely excreted *via* renal filtration and hepatobiliary pathways as the intact complex.

DISCUSSION

In this study, the well-described zinc binding unit, BPEN, was attached to a previously reported stable Mn^{2+} complex, MnPyC3A,[20] and the resulting complex was evaluated as a responsive MR imaging agent for the detection of Zn^{2+} released from the tissue *in vivo*. This responsive agent, like prior Gd-based zinc-responsive agents, showed only a modest increase in r_1 relaxivity in the presence of Zn^{2+} or HSA alone, but when both were present, a ternary complex is formed and r_1 is significantly increased. Although the primary protein contributing to the increase in relaxivity in this work is albumin, it is important to denote that other noncovalent interactions with proteins found in the plasma may also contribute to the relaxivity increase. The goal of this study was (1) to create a Mn-based Zn^{2+}-responsive MRI CA, (2) to demonstrate its utility *in vivo* for detection of Zn^{2+} secretion from tissues in live animals, (3) to evaluate the stability of MnPyC3A–BPEN against transmetalation by Zn^{2+}, and (4) to determine the tissue biodistribution and excretion pathways of this new agent. The results show that MnPyC3A–BPEN not only detects Zn^{2+} secretion from the pancreas and prostate in mice by MRI but the BPEN unit also increases the kinetic inertness of the complex toward transmetalation by Zn^{2+} and transchelation by HSA. T_1-weighted MR images of live animals showed contrast enhancement in the pancreas and prostate only after the injection of glucose to stimulate Zn^{2+} secretion from these tissues, similar to the contrast observed previously with the most effective Gd-based Zn^{2+}-responsive agents.[45,46,52] Moreover, the tissue-biodistribution and excretory characterization studies both indicate that MnPyC3A–BPEN is excreted intact via both renal filtration and hepatobiliary clearance pathways. The later clearance pathway may reflect a combination of its slightly more lipophilic character[64] plus its negative charge for transport into hepatocytes by a family of organic anion transporting proteins expressed on the sinusoidal membrane of hepatocytes.[65]

Possible limitations include: (1) the consideration that when using Zn^{2+} as a biomarker for malignant transformations, tissues may exhibit aberrant pH or oxygenation levels potentially altering the binding to the compound and thus the ternary complex and (2) the use of only

male animals in the imaging studies. We observed that in pH aberrant environments (pH 6 or 8) the binding mechanism to Zn^{2+} may be slightly affected (Table S1) and should be considered when imaging zinc content and secretion in cancer tissues. Although there could potentially be gender differences in the secretory capacity of the pancreas, we used only male mice here so that both the pancreas and prostate could be studied in the same imaging setting. Given current concerns about the use of Gd-based CAs in humans,[14] hopefully, this study will help advance discoveries of other Mn-based Zn^{2+}-responsive MRI agents for imaging glucose-stimulated zinc secretion in different organs so that one can image the pathological effects associated with dysregulation in Zn^{2+} homeostasis.

CONCLUSIONS

In summary, MnPyC3A–BPEN offers an alternative to similar Gd-based zinc-sensitive MRI CAs for the *in vivo* detection of GSZS from pancreatic β-cells and from the prostate by MRI. This new sensor also offers superior kinetic inertness toward Zn^{2+} transmetalation compared to other GBCAs based upon linear amine ligand platforms. Given that MnPyC3A appears to be moving toward clinical trials as an alternative to GBCA,[66] MnPyC3A–BPEN may also have a translational value for the early detection of prostate cancer and for monitoring β-cell function during the development of type 2 diabetes.

EXPERIMENTAL SECTION

Synthesis.

Refer to Scheme S1 for structures. To a stirred solution of **1** (0.592 g, 1 mmol), (7-azabenzotriazolyl-1-yloxy)trispyrrilodino phosphonium hexaflurophosphate (1.042 g, 2 mmol) and *N,N*-diisopropylethylamine (1.29 g.10 mmol) in 5 mL of anhydrous *N,N*-dimethylformamide was added *N′,N′*-bis(pyridine-2-ylmethyl)ethane-1,2-diamine (0.482 g, 2 mmol). The mixture was stirred at room temperature for 2 h; 100 mL of dichloromethane was added and washed with water (50 mL × 3) followed by brine (100 mL). The organic layer was dried over Na_2SO_4 and concentrated to a brown oil. The crude product was purified by flash chromatography (alumina, 5% MeOH in dichloromethane) to yield 0.490 (58.7%) g of **2** as a pale brown oil. ^{1}H NMR $CDCl_3$ 400 MHz δ: 9.15 (1H, s), 8.71 (3H, m), 8.12 (3H, t), 7.84 (2H, d), 7.60 (2H, m), 4.24 (CH_2NCH_2C, 8H, s), 3.11 (NCH_2, 10H, m), 2.99 (CH_2CHN, 4H), 1.79 ($OCCH_3$, 21H, m), 1.35 ($NCHCH_2$, 8H, s); ^{13}C NMR $CDCl_3$ 100 MHz δ: 168.8, 168.0 (CONH), 159.4, 159.0, 152.0, 143.0, 142.9, 129.8, 125.9, 124.3, 123.3 (CH–Py), 81.7 (CCH_3), 62.6, 60.9, 55.4, 52.8 (NCH_2), 26.9,25.3 (CCH_3), 24.2, 23.6 (CH_2). ESIMS positive mode *m/z* 816.1 $[M + H]^+$ calculated for $M + H^+$ $C_{45}H_{66}N_7O_7$ *m/z* 816.5.

Compound **2** (0.204 g. 0.25 mmol) was stirred in 5 mL 3N HCl for 48 h. Acid was removed *in vacuo* and the residue lyophilized to yield compound **3** as an off white solid in quantitative yield. (0.16 g). ^{1}H NMR $CDCl_3$ 400 MHz δ: 9.01 (1H, s), 8.65 (3H, d), 8.40 (3H, t), 7.98 (2H, d), 7.87 (2H, m), 4.25 (8H, s), 3.55 (6H, m), 2.91 (2H, m), 2.22 (2H, m), 1.80 (2H, m), 1.38 (2H, m), 1.23 (2H, m); ^{13}C NMR $CDCl_3$ 100 MHz δ: 169.8, 165.9, 159.4, 159.0, 152.4, 147.2, 141.3, 127.1, 126.3, 117.7, 114.8, 62.6, 55.3, 53.3, 37.4, 26.9, 24.2, 23.6. ESIMS positive mode *m/z* 648.0 $[M + H]^+$ calculated for $M + H^+$ $C_{33}H_{42}N_7O_7$ *m/z* 648.3.

Free ligand **3** (0.194 g 0.3 mmol) was dissolved in 5 mL of water and pH adjusted to 6.5, and $MnCl_2.4H_2O$ (0.059 g. 0.3 mmol) was added and pH re-adjusted to 6.5. The complex formation was monitored using LC–MS. The mixture was purified on a RP–HPLC C18 column using 50 mM ammonium acetate buffer at pH 6.5 and acetonitrile containing 5% 50 mM ammonium acetate buffer at pH 6.5 as the mobile phase to get 0.165 g (78.5%) of Mn(**3**). Mn^{2+}content: 6.6% by ICP–OES; ESIMS positive mode *m/z* 701.0 $[M + 2H]^+$ calculated for $M + 2H^+$ $C_{33}H_{40}N_7O_7Mn$ *m/z* 701.3.

In Vivo MRI.

All animal experiments were carried out following UT Southwestern guidelines for animal handling provided by the institutional animal care and use committee. Fasted male C57Bl6 mice were imaged at 4.7 *T*(Figure S3) and 9.4 *T*(Figure S4) using Varian/Agilent scanners. Mice were anesthetized with 2–5% isofluorane/oxygen mixture and their body temperature was maintained at 37 °C using a heated airflow. Two ge3d T_1-weighted scans were obtained as a baseline (TE/TR = 1.69/3.35 ms, average = 4, $\theta = 20°$, matrix 128 × 128 × 128). Mice then received 0.07 mmol/kg of either (1) MnPyC3A–BPEN plus 2.2 mmol/kg D-glucose i.p, (2) MnPyC3A×BPEN plus saline, and (3) MnPyC3A i.v. plus 2.2 mmol/kg D-glucose i.p. Following the administration of CAs, sequential 3d T_1-weighted scans were obtained for 30 ($N = 3$) or 90 min ($N = 4$) until clearance of the agent was evident. Using ImageJ, the organs of interest were identified and ROIs were measured and normalized against ROIs drawn and measured from the back muscle found in same slice and time point. The change in the MR signal intensity is reported as a percentage compared to pre-injection scans. The area under the curve was measured over a period of 1–16 min postcontrast administration using GraphPad Prism 7 software, statistical significance was evaluated using unpaired two-tailed *t*-tests to compare between agents, *p*-values < 0.05 were considered significant.

Biodistribution by ICP–MS and LC–MS.

Biodistribution studies were performed in mice fasted for at least 12 h by injecting 0.07 mmol/kg of Mn(PyC3A–BPEN), 0.04 mmol/kg $MnCl_2$, or saline i.v. followed by an immediate injection of 2.2 mmol/kg D-glucose i.p. The kidney, brain, liver, heart, spleen, muscle, pancreas, and prostate were resected 15 and 90 min postinjection to monitor long-term accumulation/excretion. The tissue was digested by dissolving in 2 mL of freshly prepared aqua regia (1:3 mixture of nitric acid and hydrochloric acid) and lysing for 24 h. The lysed tissue samples were heated at 120 °C till the aqua regia evaporated. The residual digested tissue was dissolved in 0.5N HCl by sonicating for 30 min. The samples were centrifuged at 4000*g* for 5 min to eliminate any residues. The resultant sample solutions (10 μL) were diluted up to 5 mL with 4% HNO_3 and analyzed by ICP–MS for Mn^{2+} ion concentration. Along with collecting tissue, urine and bile were collected by carefully extracting at least 20 μL of fluid from both organs using a 30 G needle and a 1 mL syringe. The fluids were immediately inserted into a LC–MS and the traces were obtained. Additionally, Mn concentration was obtained by ICP–MS. The bile and urine of animals receiving only saline i.v. and 2.2 mmol/Kg D-glucose i.p. were collected for LC–MS trace composition analysis of background fluid. Naïve urine and bile were spiked with Mn(PyC3A–BPEN) at the concentrations obtained from ICP–MS of the injected animals.

These spiked fluids were then inserted into a LC–MS and the traces were obtained and compared.

Supplementary Material

Refer to Web version on PubMed Central for supplementary material.

ACKNOWLEDGMENTS

We thank the core facilities at UTD for providing access to the ICP–MS spectrometer for these measurements and the Simmons Cancer Center at UT Southwestern Medical Center for support of the animal MRI scanners.

Funding

The work was supported by grants from the NIH (DK095416 and EB-015908), the Cancer Prevention and Research Institute of Texas (RP180178), and the Robert A. Welch Foundation (AT-584).

REFERENCES

(1). Frayne R; Goodyear BG; Dickhoff P; Lauzon ML; Sevick RJ Magnetic Resonance Imaging at 3.0 Tesla: Challenges and Advantages in Clinical Neurological Imaging. Invest. Radiol 2003, 38, 385. [PubMed: 12821852]

(2). Smith-Bindman R; Miglioretti DL; Johnson E; Lee C; Feigelson HS; Flynn M; Greenlee RT; Kruger RL; Hornbrook MC; Roblin D; Solberg LI; Vanneman N; Weinmann S; Williams AE Use of Diagnostic Imaging Studies and Associated Radiation Exposure For Patients Enrolled in Large Integrated Healthcare Systems, 1996–2010. JAMA, J. Am. Med. Assoc 2012, 307, 2400–2409.

(3). Kupersmith MJ; Alban T; Zeiffer B; Lefton D Contrast-enhanced MRI in Acute Optic Neuritis: Relationship to Visual Performance. Brain 2002, 125, 812–822. [PubMed: 11912114]

(4). Chen L; Yang Q; Bao J; Liu D; Huang X; Wang J Direct Comparison of PET/CT and MRI to Predict the Pathological Response to Neoadjuvant Chemotherapy in Breast Cancer: A Meta-Analysis. Sci. Rep 2017, 7, 8479. [PubMed: 28814795]

(5). Merbach AE; Helm L; Toth E The Chemistry of Contrast Agents in Medical Magnetic Resonance Imaging; 2nd ed.; John Wiley & Sons: United Kingdom, 2013.

(6). Ichikawa T; Haradome H; Hachiya J; Nitatori T; Araki T Diffusion-Weighted MR Imaging with a Single-Shot Echoplanar Sequence: Detection and Characterization of Focal Hepatic Lesions. Am. J. Roentgenol 1998, 170, 397–402. [PubMed: 9456953]

(7). Pagani E; Bizzi A; Di Salle F; De Stefano N; Filippi M Basic Concepts of Advanced MRI Techniques. Neurol. Sci 2008, 29, 290. [PubMed: 18941716]

(8). Onishi N; Kataoka M; Kanao S; Sagawa H; Iima M; Nickel MD; Toi M; Togashi K Ultrafast Dynamic Contrast-Enhanced Mri of the Breast Using Compressed Sensing: Breast Cancer Diagnosis Based on Separate Visualization of Breast Arteries and Veins. J. Magn. Reson. Imag 2018, 47, 97–104.

(9). Jones KM; Pollard AC; Pagel MD Clinical Applications of Chemical Exchange Saturation Transfer (CEST) MRI. J. Magn. Reson. Imag 2018, 47, 11–27.

(10). De León-Rodríguez LM; Martins AF; Pinho MC; Rofsky NM; Sherry AD Basic MR Relaxation Mechanisms and Contrast Agent Design. J. Magn. Reson. Imag 2015, 42, 545–565.

(11). Abujudeh HH; Rolls H; Kaewlai R; Agarwal S; Gebreananya ZA; Saini S; Schaefer PW; Kay J Retrospective Assessment of Prevalence of Nephrogenic Systemic Fibrosis (NSF) after Implementation of a New Guideline for the Use of Gadobenate Dimeglumine as a Sole Contrast Agent for Magnetic Resonance Examination in Renally Impaired Patients. J. Magn. Reson. Imag 2009, 30, 1335–1340.

(12). Reilly RF Risk for Nephrogenic Systemic Fibrosis with Gadoteridol (ProHance) in Patients Who Are on Long-Term Hemodialysis. Clin. J. Am. Soc. Nephrol 2008, 3, 747–751. [PubMed: 18287249]

(13). Rofsky NM; Sherry AD; Lenkinski RE Nephrogenic Systemic Fibrosis: A Chemical Perspective. Radiology 2008, 247, 608–612. [PubMed: 18487530]

(14). Stojanov D; Aracki-Trenkic A; Benedeto-Stojanov D Gadolinium Deposition within the Dentate Nucleus and Globus Pallidus after Repeated Administrations of Gadolinium-Based Contrast Agents–Current Status. Neuroradiology 2016, 58, 433–441. [PubMed: 26873830]

(15). Gianolio E; Bardini P; Arena F; Stefania R; Di Gregorio E; Iani R; Aime S Gadolinium Retention in the Rat Brain: Assessment of the Amounts of Insoluble Gadolinium-Containing Species and Intact Gadolinium Complexes after Repeated Administration of Gadolinium-Based Contrast Agents. Radiology 2017, 285, 839–849. [PubMed: 28873047]

(16). Brücher E Kinetic Stabilities of Gadolinium(III) Chelates Used as MRI Contrast Agents. In Contrast Agents I; Krause PDW, Ed.; Topics in Current Chemistry; Springer Berlin Heidelberg, 2002; pp 103–122.

(17). Brücher E; Tircsó G; Baranyai Z; Kovács Z; Sherry AD Stability and Toxicity of Contrast Agents. In The Chemistry of Contrast Agents in Medical Magnetic Resonance Imaging; Merbach A, Helm L, Tóth É, Eds.; John Wiley & Sons, Ltd: United Kingdom, 2013; pp 157–208.

(18). Caravan P; Farrar CT; Frullano L; Uppal R Influence of Molecular Parameters and Increasing Magnetic Field Strength on Relaxivity of Gadolinium- and Manganese-Based T1 Contrast Agents. Contrast Media Mol. Imaging 2009, 4, 89–100. [PubMed: 19177472]

(19). Madejczyk MS; Boyer JL; Ballatori N Hepatic Uptake and Biliary Excretion of Manganese in the Little Skate, Leucoraja Erinacea. Comp. Biochem. Physiol. C Comp. Pharmacol. Toxicol 2009, 149, 566–571.

(20). Gale EM; Atanasova IP; Blasi F; Ay I; Caravan P A Manganese Alternative to Gadolinium for MRI Contrast. J. Am. Chem. Soc 2015, 137, 15548–15557. [PubMed: 26588204]

(21). Ali SF; Duhart HM; Newport GD; Lipe GW; Slikker W Manganese-Induced Reactive Oxygen Species: Comparison between Mn+2 and Mn+3. Neurodegeneration 1995, 4, 329–334. [PubMed: 8581566]

(22). Patel RP; McAndrew J; Sellak H; White CR; Jo H; Freeman BA; Darley-Usmar VM Biological Aspects of Reactive Nitrogen Species. Biochim. Biophys. Acta Bioenerg 1999, 1411, 385–400.

(23). Martinez-Finley EJ; Gavin CE; Aschner M; Gunter TE Manganese Neurotoxicity and the Role of Reactive Oxygen Species. Free Radic. Biol. Med 2013, 62, 65–75. [PubMed: 23395780]

(24). Liu G-F; Filipović M; Heinemann FW; Ivanović-Burmazović I Seven-Coordinate Iron and Manganese Complexes with Acyclic and Rigid Pentadentate Chelates and Their Superoxide Dismutase Activity. Inorg. Chem 2007, 46, 8825–8835. [PubMed: 17880209]

(25). Miriyala S; Spasojevic I; Tovmasyan A; Salvemini D; Vujaskovic Z; St. Clair D; Batinic-Haberle I. Manganese Super-oxide Dismutase, MnSOD and Its Mimics. Biochim. Biophys. Acta (BBA)–Mol. Basis Dis 2012, 1822, 794–814.

(26). Karlsson JOG; Ignarro LJ; Lundström I; Jynge P; Almén T Calmangafodipir [Ca4Mn(DPDP)5], Mangafodipir (MnDPDP) and MnPLED with Special Reference to Their SOD Mimetic and Therapeutic Properties. Drug Discov. Today 2015, 20, 411–421. [PubMed: 25463039]

(27). Johnson DA; Nelson PG Factors Determining the Ligand Field Stabilization Energies of the Hexaaqua 2+ Complexes of the First Transition Series and the Irving-Williams Order. Inorg. Chem 1995, 34, 5666–5671.

(28). Drahoš B; Kubíček V; Bonnet CS; Hermann P; Lukeš I; Tóth É Dissociation Kinetics of Mn2+ Complexes of NOTA and DOTA. Dalton Trans 2011, 40, 1945–1951. [PubMed: 21274464]

(29). Drahoš B; Lukeš I; Tóth É Manganese(II) Complexes as Potential Contrast Agents for MRI. Eur. J. Inorg. Chem 2012, 2012, 1975–1986.

(30). Loving GS; Mukherjee S; Caravan P Redox-Activated Manganese-Based MR Contrast Agent. J. Am. Chem. Soc 2013, 135, 4620–4623. [PubMed: 23510406]

(31). Molnár E; Camus N; Patinec V; Rolla GA; Botta M; Tircsó G; Kálmán FK; Fodor T; Tripier R; Platas-Iglesias C Picolinate-Containing Macrocyclic Mn2+ Complexes as Potential MRI Contrast Agents. Inorg. Chem 2014, 53, 5136–5149. [PubMed: 24773460]

(32). Drahoš B; Herchel R; Trávníček Z Structural and Magnetic Properties of Heptacoordinated Mn II Complexes Containing a 15-Membered Pyridine-Based Macrocycle and Halido/Pseudohalido Axial Coligands. RSC Adv 2016, 6, 34674–34684.

(33). Forgács A; Pujales-Paradela R; Regueiro-Figueroa M; Valencia L; Esteban-Gómez D; Botta M; Platas-Iglesias C Developing the Family of Picolinate Ligands for Mn2+ Complexation. Dalton Trans 2017, 46, 1546–1558. [PubMed: 28091671]

(34). Forgács A; Tei L; Baranyai Z; Esteban-Gómez D; Platas-Iglesias C; Botta M Optimising the Relaxivities of Mn2+ Complexes by Targeting Human Serum Albumin (HSA). Dalton Trans 2017, 46, 8494–8504. [PubMed: 28632276]

(35). Pota K; Garda Z; Kálmán FK; Barriada JL; Esteban-Gómez D; Platas-Iglesias C; Tóth I; Brücher E; Tircsó G Taking the next Step toward Inert Mn2+ Complexes of Open-Chain Ligands: The Case of the Rigid PhDTA Ligand. New J. Chem 2018, 42, 8001–8011.

(36). Laine S; Bonnet CS; Kálmán FK; Garda Z; Pallier A; Caillé F; Suzenet F; Tircsó G; Tóth É Mn2+ Complexes of Open-Chain Ligands with a Pyridine Backbone: Less Donor Atoms Lead to Higher Kinetic Inertness. New J. Chem 2018, 42, 8012–8020.

(37). Le Fur M; Molnár E; Beyler M; Fougère O; Esteban-Gómez D; Rousseaux O; Tripier R; Tircsó G; Platas-Iglesias C Expanding the Family of Pyclen-Based Ligands Bearing Pendant Picolinate Arms for Lanthanide Complexation. Inorg. Chem 2018, 57, 6932–6945. [PubMed: 29846067]

(38). Garda Z; Molnár E; Kálmán FK; Botár R; Nagy V; Baranyai Z; Brücher E; Kovács Z; Tóth I; Tircsó G Effect of the Nature of Donor Atoms on the Thermodynamic, Kinetic and Relaxation Properties of Mn(II) Complexes Formed With Some Trisubstituted 12-Membered Macrocyclic Ligands. Front. Chem 2018, 6, 232. [PubMed: 30151358]

(39). Gale EM; Wey HY; Ramsay I; Yen YF; Sosnovik DE; Caravan P A Manganese-Based Alternative to Gadolinium: Contrast-Enhanced MR Angiography, Excretion, Pharmacokinetics, and Metabolism. Radiology 2018, 286, 865–872. [PubMed: 29117483]

(40). Zhang X.-a.; Lovejoy KS; Jasanoff A; Lippard SJ. Water-Soluble Porphyrins as a Dual-Function Molecular Imaging Platform for MRI and Fluorescence Zinc Sensing. Proc. Natl. Acad. Sci. U.S.A 2007, 104, 10780–10785. [PubMed: 17578918]

(41). Lee T; Zhang X.-a.; Dhar S; Faas H; Lippard SJ; Jasanoff A. In Vivo Imaging with a Cell-Permeable Porphyrin-Based MRI Contrast Agent. Chem. Biol 2010, 17, 665–673. [PubMed: 20609416]

(42). Esqueda AC; López JA; Andreu-de-Riquer G; Alvarado-Monzón JC; Ratnakar J; Lubag AJM; Sherry AD; De León-Rodríguez LM A New Gadolinium-Based MRI Zinc Sensor. J. Am. Chem. Soc 2009, 131, 11387–11391. [PubMed: 19630391]

(43). Lubag AJM; De Leon-Rodriguez LM; Burgess SC; Sherry AD Noninvasive MRI of Beta-Cell Function Using a Zn2+-Responsive Contrast Agent. Proc. Natl. Acad. Sci. U.S.A 2011, 108, 18400–18405. [PubMed: 22025712]

(44). León-Rodríguez LMD; Lubag AJM; López JA; Andreu-de-Riquer G; Alvarado-Monzón JC; Sherry AD A Second Generation MRI Contrast Agent for Imaging Zinc Ions in Vivo. MedChemComm 2012, 3, 480–483. [PubMed: 24013159]

(45). Martins AF; Clavijo Jordan V; Bochner F; Chirayil S; Paranawithana N; Zhang S; Lo S-T; Wen X; Zhao P; Neeman M; Sherry AD Imaging Insulin Secretion from Mouse Pancreas by MRI Is Improved by Use of a Zinc-Responsive MRI Sensor with Lower Affinity for Zn2+ Ions. J. Am. Chem. Soc 2018, 140, 17456–17464. [PubMed: 30484648]

(46). Clavijo Jordan MV; Lo ST; Chen S; Preihs C; Chirayil S; Zhang S; Kapur P; Li WH; De Leon-Rodriguez LM; Lubag AJ; Rofsky NM; Sherry AD Zinc-Sensitive MRI Contrast Agent Detects Differential Release of Zn(II) Ions from the Healthy vs. Malignant Mouse Prostate. Proc. Natl. Acad. Sci. U.S.A 2016, 113, E5464–E5471. [PubMed: 27562169]

(47). Lo S-T; Martins AF; Jordan VC; Sherry AD Zinc as an Imaging Biomarker of Prostate Cancer. Isr. J. Chem 2017, 57, 854–861. [PubMed: 30319140]

(48). Major JL; Boiteau RM; Meade TJ Mechanisms of ZnII-Activated Magnetic Resonance Imaging Agents. Inorg. Chem 2008, 47, 10788–10795. [PubMed: 18928280]

(49). Mishra A; Logothetis NK; Parker D Critical In Vitro Evaluation of Responsive MRI Contrast Agents for Calcium and Zinc. Chem.— Eur J 2011, 17, 1529–1537. [PubMed: 21268155]

(50). Bonnet CS; Caillé F; Pallier A; Morfin J-F; Petoud S; Suzenet F; Tóth É Mechanistic Studies of Gd3+-Based MRI Contrast Agents for Zn2+ Detection: Towards Rational Design. Chem.— Eur J 2014, 20, 10959–10969. [PubMed: 25116889]

(51). Stasiuk GJ; Minuzzi F; Sae-Heng M; Rivas C; Juretschke H-P; Piemonti L; Allegrini PR; Laurent D; Duckworth AR; Beeby A; Rutter GA; Long NJ Dual-Modal Magnetic Resonance/Fluorescent Zinc Probes for Pancreatic β-Cell Mass Imaging. Chem.— Eur J 2015, 21, 5023–5033. [PubMed: 25736590]

(52). Yu J; Martins AF; Preihs C; Clavijo Jordan V; Chirayil S; Zhao P; Wu Y; Nasr K; Kiefer GE; Sherry AD Amplifying the Sensitivity of Zinc(II) Responsive MRI Contrast Agents by Altering Water Exchange Rates. J. Am. Chem. Soc 2015, 137, 14173–14179. [PubMed: 26462412]

(53). Gonzalez G; Powell DH; Tissieres V; Merbach AE Water-Exchange, Electronic Relaxation, and Rotational Dynamics of the MRI Contrast Agent [Gd(DTPA-BMA)(H2O)] in Aqueous Solution : A Variable Pressure, Temperature, and Magnetic Field 17O NMR Study. J. Phys. Chem 1994, 98, 53–59.

(54). Powell DH; Dhubhghaill OMN; Pubanz D; Helm L; Lebedev YS; Schlaepfer W; Merbach AE Structural and Dynamic Parameters Obtained from 17O NMR, EPR, and NMRD Studies of Monomeric and Dimeric Gd3+ Complexes of Interest in Magnetic Resonance Imaging: An Integrated and Theoretically Self-Consistent Approach1. J. Am. Chem. Soc 1996, 118, 9333–9346.

(55). Martins AF; Morfin J-F; Geraldes CFGC; Tóth É Gd3+ Complexes Conjugated to Pittsburgh Compound B: Potential MRI Markers of β-Amyloid Plaques. J. Biol. Inorg Chem 2013, 19, 281–295. [PubMed: 24297602]

(56). Martins AF; Oliveira AC; Morfin J-F; Laurents DV; Tóth É; Geraldes CFGC Associating a Negatively Charged GdDOTA-Derivative to the Pittsburgh Compound B for Targeting Aβ Amyloid Aggregates. J. Biol. Inorg. Chem 2016, 21, 83–99. [PubMed: 26613605]

(57). Stewart AJ; Blindauer CA; Berezenko S; Sleep D; Sadler PJ Interdomain Zinc Site on Human Albumin. Proc. Natl. Acad. Sci. U.S.A 2003, 100, 3701–3706. [PubMed: 12598656]

(58). Livieri M; Mancin F; Saielli G; Chin J; Tonellato U Mimicking Enzymes: Cooperation between Organic Functional Groups and Metal Ions in the Cleavage of Phosphate Diesters. Chem. Weinh. Bergstr. Ger 2007, 13, 2246–2256.

(59). Lu J; Stewart AJ; Sadler PJ; Pinheiro TJT; Blindauer CA Albumin as a Zinc Carrier: Properties of Its High-Affinity Zinc-Binding Site. Biochem. Soc. Trans 2008, 36, 1317–1321. [PubMed: 19021548]

(60). Botár R; Molnár E; Trencsényi G; Kiss J; Kálmán FK; Tircsó G Stable and Inert Mn(II)-Based and PH-Responsive Contrast Agents. J. Am. Chem. Soc 2020, 142, 1662–1666. [PubMed: 31927927]

(61). Aime S; Canton S; Geninatti Crich S; Terreno E 1H and 17O Relaxometric Investigations of the Binding of Mn(II) Ion to Human Serum Albumin. Magn. Reson. Chem 2002, 40, 41–48.

(62). Clavijo Jordan V; Al-Ebraheem A; Geraki K; Dao E; Martins AF; Chirayil S; Farquharson M; Sherry AD Synchrotron Radiation X-Ray Fluorescence Elemental Mapping in Healthy versus Malignant Prostate Tissues Provides New Insights into the Glucose-Stimulated Zinc Trafficking in the Prostate As Discovered by MRI. Inorg. Chem 2019, 58, 13654–13660. [PubMed: 31260276]

(63). Yuan Y; Wei Z; Chu C; Zhang J; Song X; Walczak P; Bulte JWM Development of Zinc-Specific ICEST MRI as an Imaging Biomarker for Prostate Cancer. Angew. Chem. Int. Ed 2019, 58, 15512–15517.

(64). Ghibellini G; Leslie EM; Brouwer KLR Methods To Evaluate Biliary Excretion of Drugs in Humans: An Updated Review. Mol. Pharm 2006, 3, 198–211. [PubMed: 16749853]

(65). Kalliokoski A; Niemi M Impact of OATP Transporters on Pharmacokinetics. Br. J. Pharmacol 2009, 158, 693–705. [PubMed: 19785645]

(66). Erstad DJ; Ramsay IA; Jordan VC; Sojoodi M; Fuchs BC; Tanabe KK; Caravan P; Gale EM Tumor Contrast Enhancement and Whole-Body Elimination of the Manganese-Based Magnetic Resonance Imaging Contrast Agent Mn-PyC3A. Invest. Radiol 2019, 54, 697–703. [PubMed: 31356382]

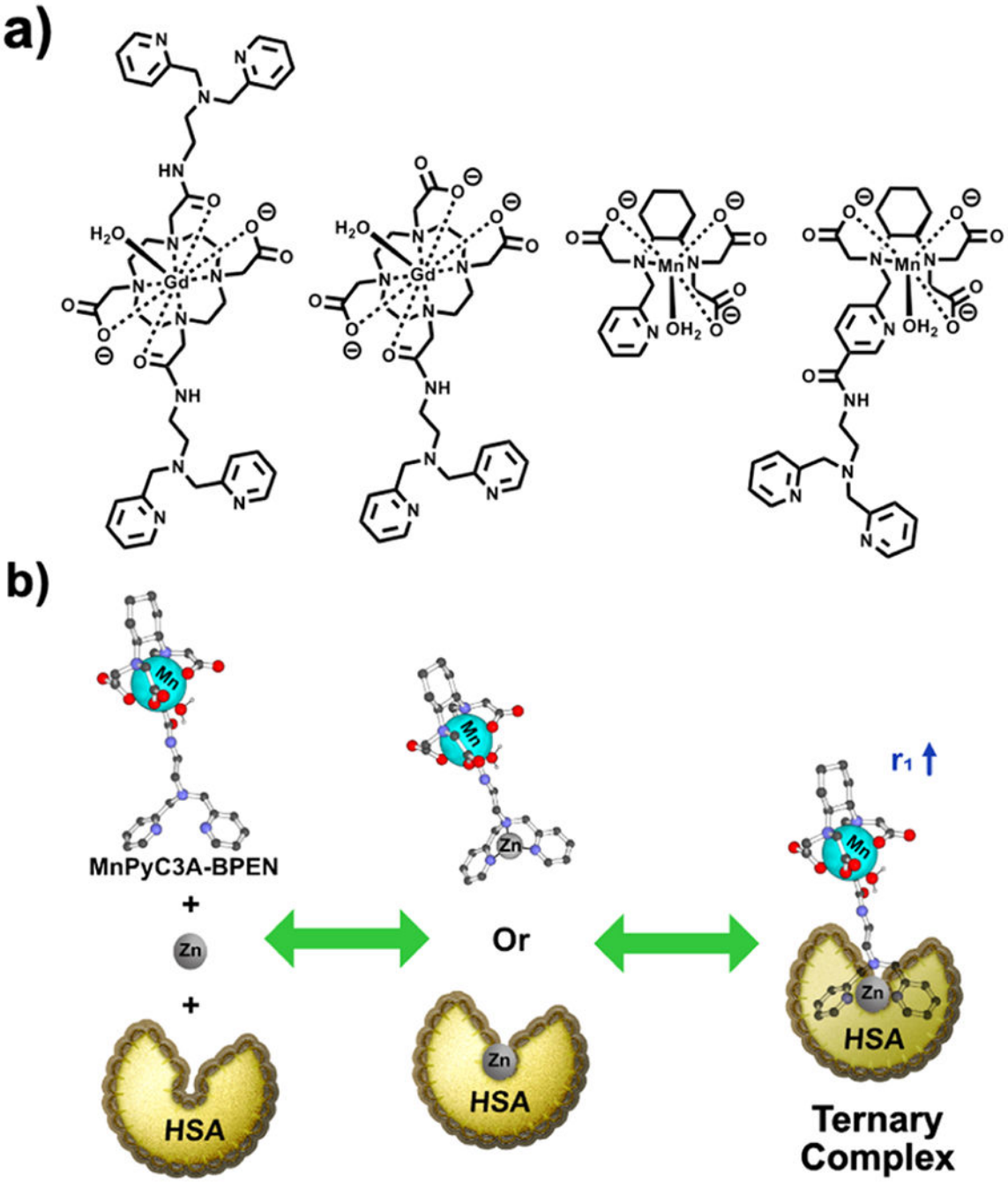

Figure 1.

Chemical structures and mechanisms for sensitive detection of Zn^{2+} in tissues. (a) GdDOTA–diBPEN, GdDO3A–BPEN, the parent MnPyC3A compound, and MnPyC3A–BPEN. (b) Mechanism of contrast enhancement involves binding of Zn^{2+} to the agent, followed by the agent-Zn^{2+} complex forming a ternary complex with albumin.

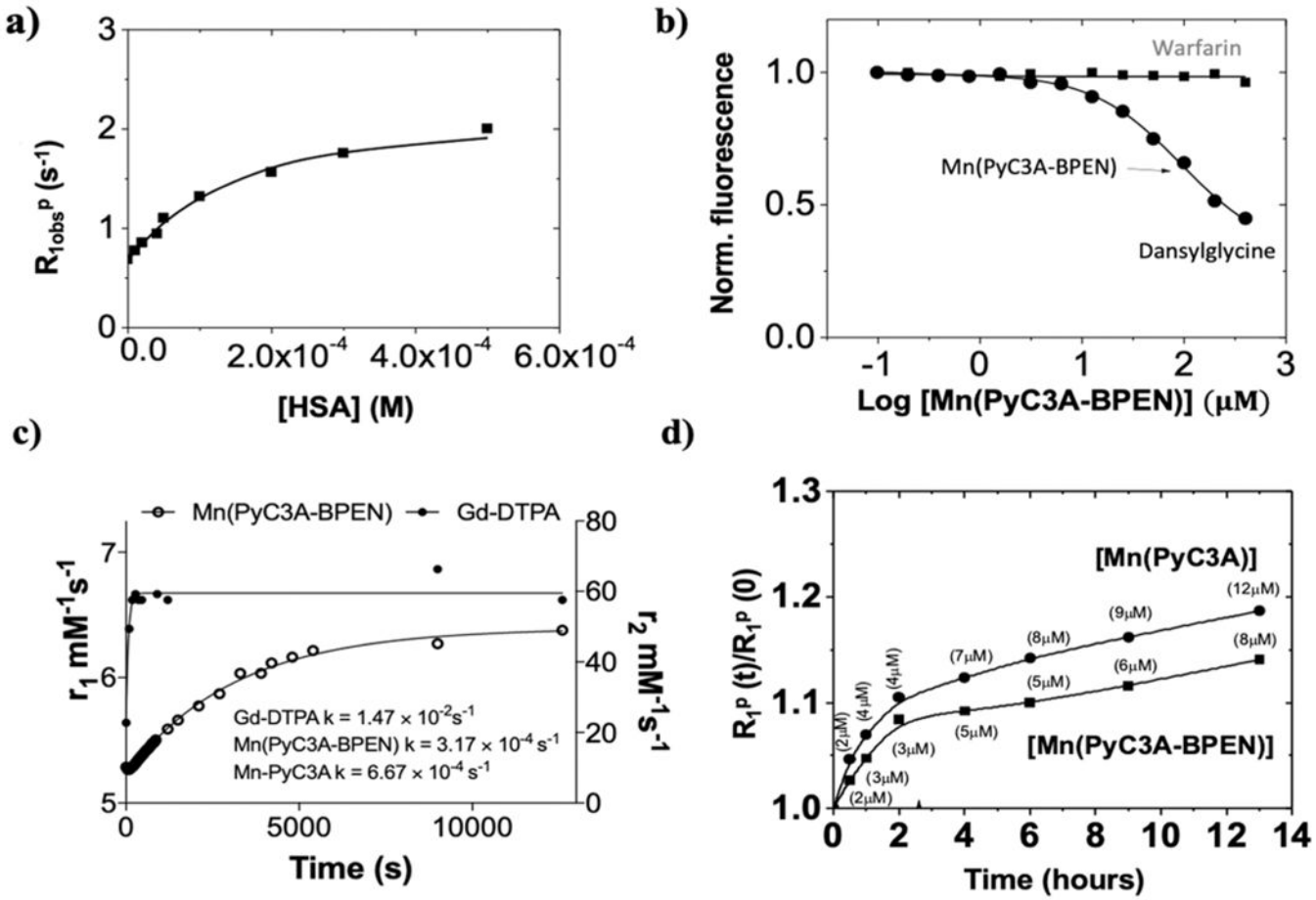

Figure 2.

Relaxometry and binding characteristics of MnPyC3A-BPEN. (a) PRE titrations of MnPyC3A–BPEN (0.1 mM) as a function of increasing [HSA]. [Zn^{2+}] was held constant (0.6 mM, equal to the highest concentration of HSA) in each titration. All measurements were performed at 20 MHz, 310 K in 100 mM Tris buffer at pH 7. (b) Competition binding curve for the determination of the MnPyC3A–BPEN·Zn^{2+} binding dissociation constants with HSA with dansylglycine (drug site 2) and warfarin (drug site 1). (c) Transmetalation studies. MnPyC3A–BPEN and GdDTPA were separately incubated with 25 mol excess Zn^{2+} at pH = 6 and the T_1 of water protons was measured using a mq60 relaxometer (B_0 = 1.5 T) over 210 min. The fitted lines reflect pseudo-first order rate constants for the dissociation of free Gd^{3+} from GdDTPA and free Mn^{2+} from MnPyC3A–BPEN. (d) Evolution of the relative water proton paramagnetic relaxation rate of 0.1 mM aqueous solutions of MnPyC3A–BPEN (■) or MnPyC3A (●) in the presence of 0.6 mM of HSA. The plots show changes in R_1 (at 23 MHz) for 1 mM samples of each agent over time, pH 7.2 in TRIS buffer, 310 K. The concentration labels reflect the calculated [Mn^{2+}] transchelated from each complex to HSA.

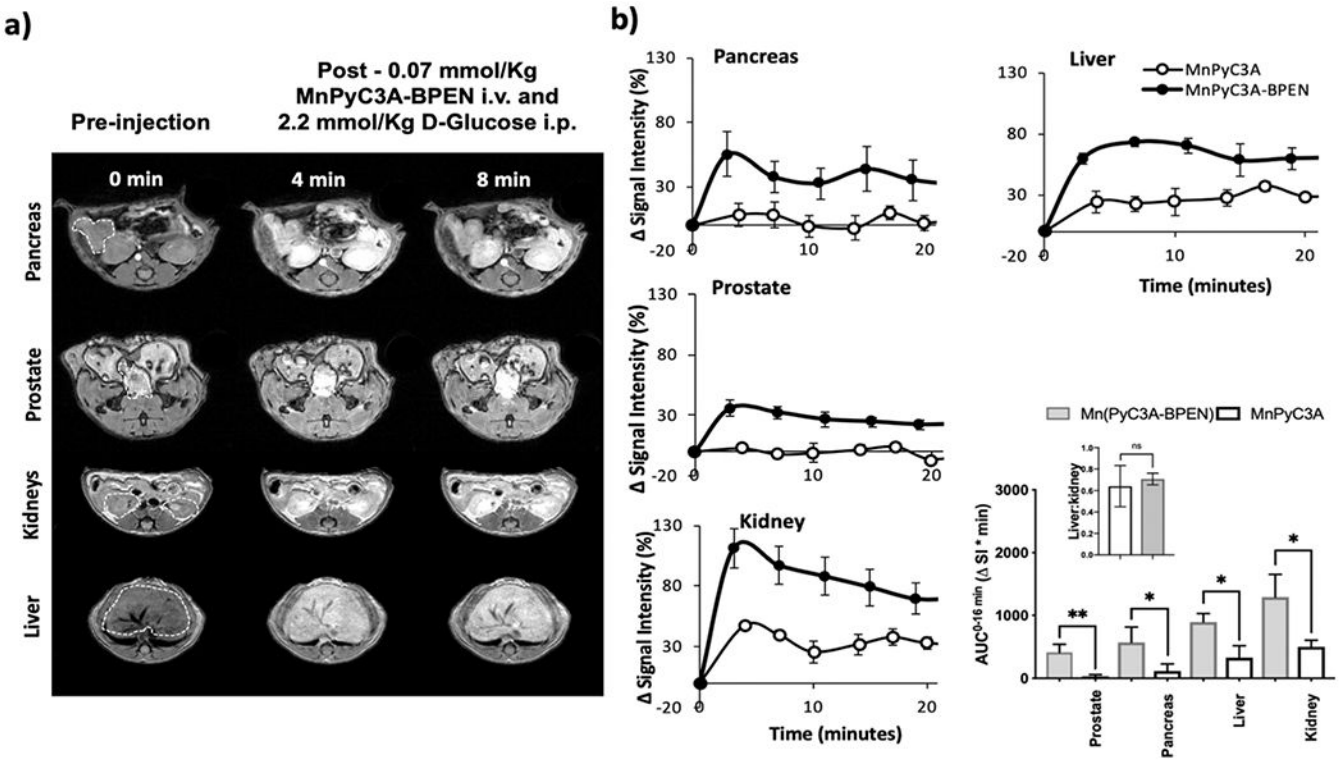

Figure 3.

Imaging Zn^{2+} secretion from tissues *in vivo* by MRI at 9.4 T. (a) T_1-weighted images (3D gradient echo TE/TR = 1.69/3.35 ms, averages = 4, $\theta = 20°$) of fasted C57Bl6 male mice after receiving 0.07 mmol/kg MnPyC3A–BPEN i.v. and 2.2 mmol/kg glucose i.p. to stimulate the release of zinc from secretory organs. (b) Quantitative changes in signal intensity in each organ normalized to muscle after administration of 0.07 mmol/kg MnPyC3A–BPEN or non-zinc sensitive control MnPyC3A i.v. and 2.2 mmol/kg glucose i.p. ($N = 3$). Integrated normalized signal intensity profiles as $AUC^{0–16\ min}$ for each agent and each organ. Bars represent standard error of the mean; *p value < 0.05, **p value < 0.01.

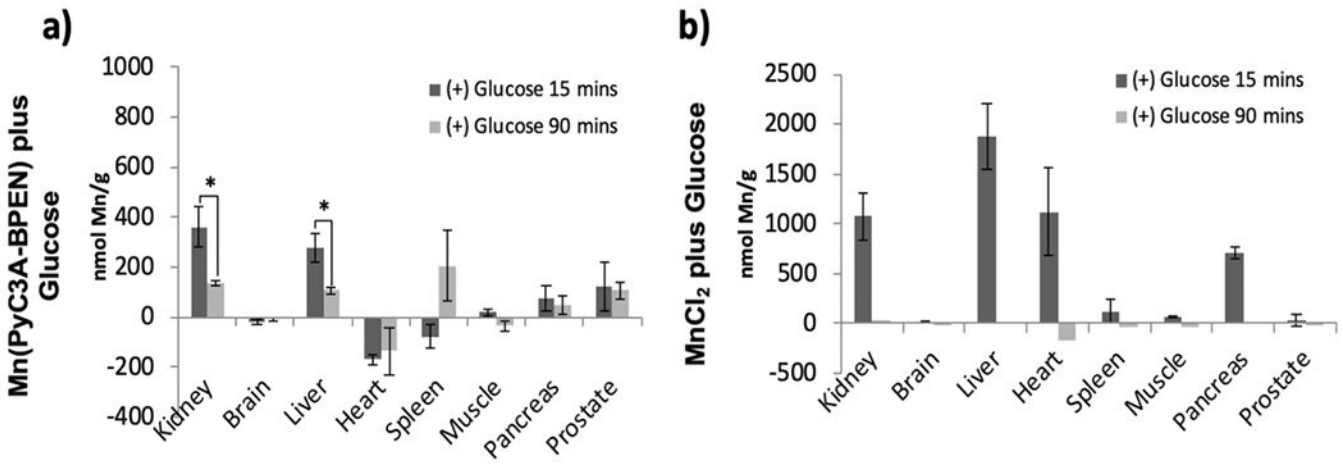

Figure 4.

Manganese content as measured by ICP–MS in organs of mice after receiving either (a) MnPyC3A–BPEN plus glucose or (b) $MnCl_2$ plus glucose. Animals were sacrificed 15 or 90 min postinjection ($N = 3$ each group). *$p < 0.05$.

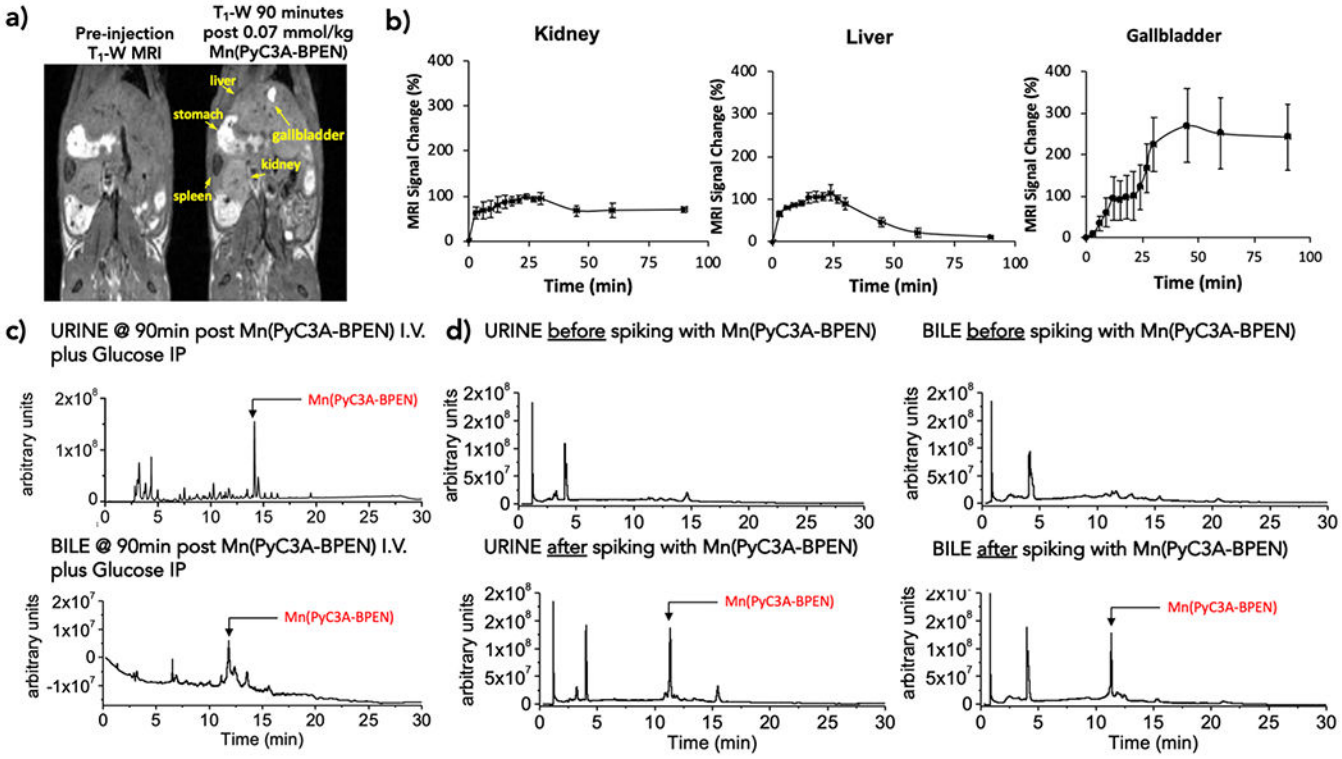

Figure 5.

MnPyC3A–BPEN excretion profiles. (a) Coronal T_1-weighted MR images of a mouse pre- and 90 min postinjection of MnPyC3A–BPEN plus glucose. (b) MR signal intensity normalized to muscle for the kidney, liver, and gallbladder as a function of time ($N = 4$). (c) LC–MS chromatogram of urine and bile collected 90 min postinjection. (d) LC–MS chromatogram of urine and bile before and after spiking with MnPyC3A–BPEN at concentrations measured in urine and bile samples collected 90 min post i.v. injection.

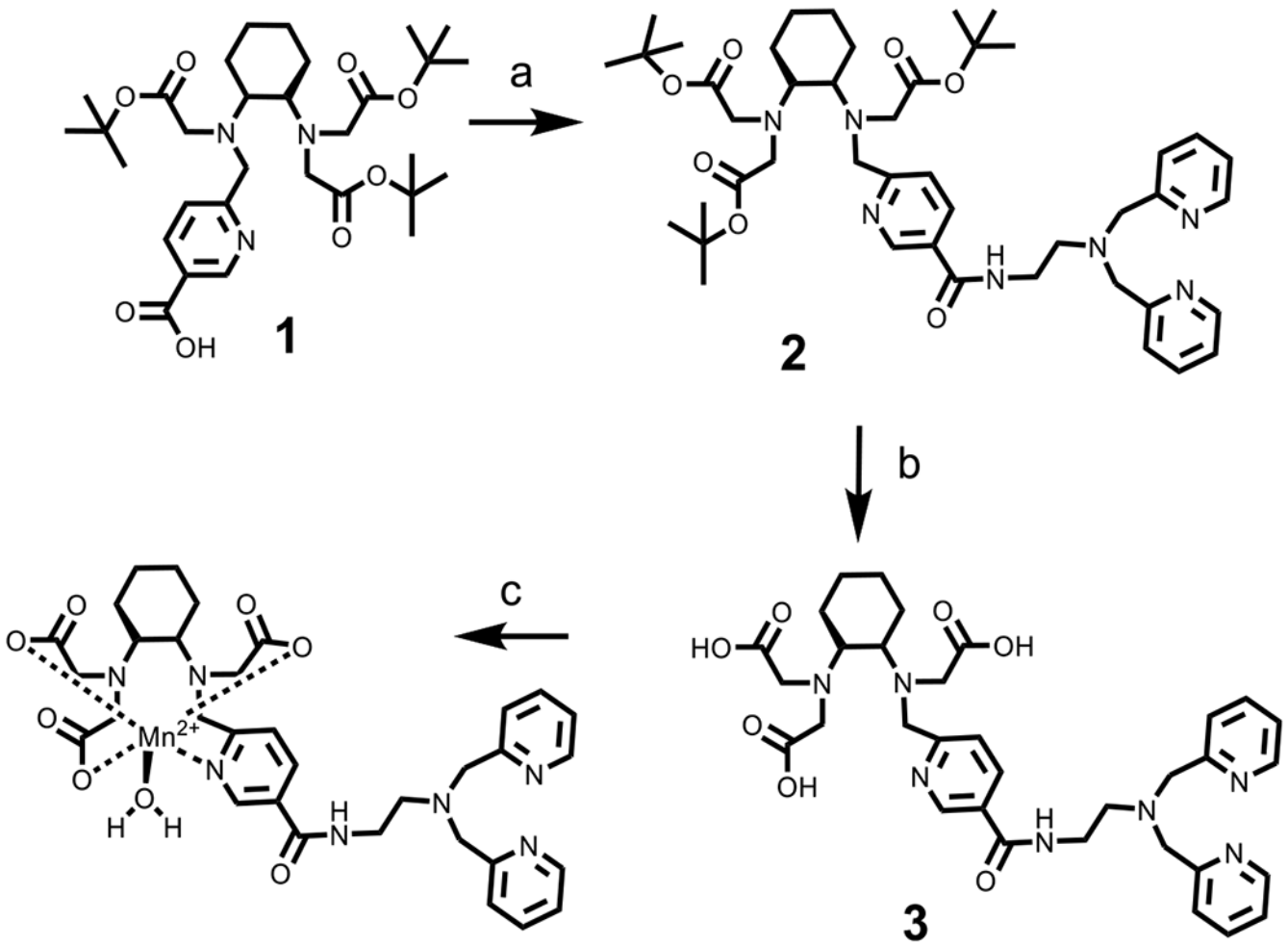

Scheme 1.

Preparation of MnPyC3A–BPEN (a) (7-Azabenzotriazol-1-yloxy)tripyrrolidinophosphonium Hexafluorophosphate (PyAOP), DMF, DIPEA, BPEN, (b) 3 M HCl, and (c) $MnCl_2$, pH 6.5

Table 1.

r_1 Relaxivities and K_D Values for Several Zinc-Sensitive MRI Agents in 100 mM Tris Buffer, 37 °C

	$r_1^{0.5T}$ (mM^{-1} s^{-1})								
CA	**No Zn^{2+}**	**(+) Zn^{2+}**	**(+) 0.6 mM HSA**	**(+) Zn^{2+} (+) 0.6 mM HSA**	**$K_{D(Zn)}$ (nM)**	**$K_{D(HSA)}$ (μM)**		**r_1^{max} (mM^{-1} s^{-1})**	**k_{ex}^{310} ($\times 10^8$ s^{-1})**
MnPyC3A-BPEN	3.7 ± 0.1	4.1 ± 0.1[a]	10.8 ± 0.1[b]	17.4 ± 0.5[b]	93 ± 4[c]	28 ± 1[d]	66 ± 7[e]	21 ± 3[d]	0.7 ± 0.2
GdDO3A-BPEN	4.8 ± 0.1	5.1 ± 0.1[a]	5.8 ± 0.1[b]	17.8 ± 0.5[b]	118 ± 3[c]	36 ± 1[d]	48 ± 6[e]	20 ± 1[d]	0.029 ± 0.001
MnPyC3A-FBP*	8.5[f]		11.4[f]	13.5[f]		0.11[i]			1.0

[a] CA/Zn = 1:1 (1 molar equivalent of Zn^{2+}).

[b] Obtained by measuring T_1 values of four different samples of sensors (0.1, 0.2, 0.3, and 0.5 mM) in 0.6 mM human serum albumin (HSA) (±0.6 mM Zn^{2+}). The r_1 values observed are only representative of these experimental conditions.

[c] Determined by competitive binding experiments with the Zn-sensitive fluorescence ligand, ZnAF–2F (see Supporting Information).

[d] Obtained by fitting proton relaxation enhancement data to equation 2 in Supporting Information.

[e] Obtained by one site competition fitting with dansylglycine.

[f] B = 1.4 T.

[g] 4.5% w/v BSA.

[h] Fibrin gel.

[i] Fluorescein-labeled fibrin binding peptide titrations.[20]

Table 2.

Number of Coordination Sites for Water Molecules (q), Enthalpy of Activation, Mn–^{17}O Hyperfine Coupling Constants ($A_O/\hbar$), and Water Exchange Rates at $T = 310$ K (k_{ex}^{310})

Cas	q calc	$\Delta H^{\ddagger}$ [kJ/mol]	A/h [x10^7 rad/s]	k_{ex}^{310} (×10^8 s^{-1})
MnPyC3A-BPEN	0.9 ± 0.2	33 ± 0.50	2.8 ± 0.10	0.7 ± 0.1
MnPyC3A*	1	37.2	2.9	1.0

Inorg Chem. Author manuscript; available in PMC 2022 February 15.